

Article

Initial Dynamics of Quantum Impurities in a Bose–Einstein Condensate

Magnus G. Skou , Thomas G. Skov , Nils B. Jørgensen  and Jan J. Arlt 

Center for Complex Quantum Systems, Department of Physics and Astronomy, Aarhus University, Ny Munkegade 120, DK-8000 Aarhus, Denmark; tg.skov@phys.au.dk (T.G.S.); nilsbyg@hotmail.com (N.B.J.); arlt@phys.au.dk (J.J.A.)

* Correspondence: magnus.skou@phys.au.dk

Abstract: An impurity immersed in a medium constitutes a canonical scenario applicable in a wide range of fields in physics. Though our understanding has advanced significantly in the past decades, quantum impurities in a bosonic environment are still of considerable theoretical and experimental interest. Here, we discuss the initial dynamics of such impurities, which was recently observed in interferometric experiments. Experimental observations from weak to unitary interactions are presented and compared to a theoretical description. In particular, the transition between two initial dynamical regimes dominated by two-body interactions is analyzed, yielding transition times in clear agreement with the theoretical prediction. Additionally, the distinct time dependence of the coherence amplitude in these regimes is obtained by extracting its power-law exponents. This benchmarks our understanding and suggests new ways of probing dynamical properties of quantum impurities.

Keywords: Bose–Einstein condensates; impurity dynamics; ramsey interferometry; polarons



Citation: Skou, M.G.; Skov, T.G.; Jørgensen, N.B.; Arlt, J.J. Initial Dynamics of Quantum Impurities in a Bose–Einstein Condensate. *Atoms* **2021**, *9*, 22. <https://doi.org/10.3390/atoms9020022>

Academic Editors: Mistakidis Simeon and Artem Volosniev

Received: 26 February 2021

Accepted: 23 March 2021

Published: 27 March 2021

Publisher's Note: MDPI stays neutral with regard to jurisdictional claims in published maps and institutional affiliations.



Copyright: © 2021 by the authors. Licensee MDPI, Basel, Switzerland. This article is an open access article distributed under the terms and conditions of the Creative Commons Attribution (CC BY) license (<https://creativecommons.org/licenses/by/4.0/>).

1. Introduction

The behavior of interacting quantum impurities is a problem of significant scientific and technological importance. Initial theoretical studies by Landau and Pekar [1] showed that a crystal lattice dresses electrons to form quasiparticles coined polarons. This intuitive model is highly successful and now serves as a basis for understanding complex condensed matter systems [2]. The concept of polarons is thus central for important technologies such as organic semiconductors [3] and high-temperature superconductors [4].

The initial dynamics of an impurity is especially intriguing. It sheds light on the intrinsic link between two-body and many-body correlations, and is key to understanding the eventual formation of a polaron. Due to the fast evolution times in most materials, this evolution has eluded observation until recently. With the advent of quantum gases, this is no longer the case since their low densities allow for long interrogation times in pure and controllable environments. Based on these systems, the spectral response and dynamical evolution of an impurity in a Fermi gas have been explored in great theoretical and experimental detail [5–13]. The mobile Bose polaron, which resembles the solid-state problem closely, has been studied spectroscopically [14–17] and its behavior has been investigated in a one-dimensional Bose gas [18,19]. However, the formation dynamics of the Bose polaron in a three-dimensional gas has remained unclear.

Here we present recent experiments, which succeed in investigating the dynamics of impurities in a Bose–Einstein condensate (BEC). This evolution of the impurities can be resolved using an interferometric sequence. The first pulse in this sequence creates an imbalanced superposition state, which evolves under the influence of interactions in the system. The second pulse then allows a measurement of the coherence between the initial state and the evolved impurity state [20]. The dynamics of the impurity can be separated into three regimes, as illustrated in Figure 1, depending on the interaction strength and the evolution time. The initial dynamics at all interaction strengths is governed

by two-body scattering between the impurity and the condensate. For short times, the two-body scattering is unitarity-limited causing the coherence to evolve universally [21]. For weak interactions, this is followed by a regime of two-body weak coupling dynamics which depends on the scattering length between the impurity state and medium state. For longer times, the dynamical behavior transitions into a regime where many-body correlations govern the evolution. For strong interactions, this regime is entered directly from universal dynamics.

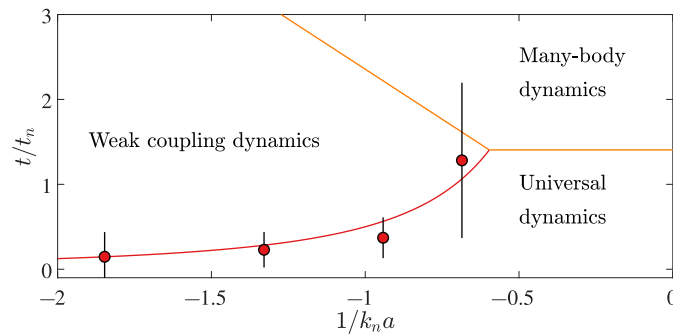


Figure 1. Regimes of impurity dynamics. Characteristic regimes of impurity dynamics as a function of the inverse interaction strength $1/k_n a$ (see text) and the evolution time t/t_n (see text). Solid lines indicate predicted transitions between the dynamical regimes. Red data points are experimentally extracted transition times and errors correspond to fit uncertainties. A similar figure was presented in Ref. [20].

This dynamical evolution was initially investigated in Ref. [20] where all three regimes were observed. Furthermore, the transition times between the regimes were obtained showing clear agreement with theoretical predictions. In this paper, we extend the analysis of the experimental observations to provide a deeper understanding of the two regimes of universal and weak coupling dynamics illustrated in Figure 1. Specifically, we discuss the transition time between them and consider the functional behavior of the coherence in the two regimes.

The paper is structured as follows. In Section 2, the experiment is briefly presented including the interferometric sequence. This is followed by the discussion of a theoretical model in Section 3. In Section 4, this model is compared with experimental observations of the coherence amplitude and phase evolution for weak and unitary interactions. The transition between the two regimes is discussed in Section 5. Finally, in Section 6 the dependence of the dynamical evolution on interaction strength is presented.

2. Experimental Details

The experiment was performed using a quantum gas of ^{39}K . The production of ^{39}K BECs has been presented in detail in Refs. [14,22] and only the relevant steps for investigating impurity dynamics are outlined here.

The experiments are based on a ^{39}K BEC in the hyperfine state $|F = 1, m_F = -1\rangle$ held in an optical dipole potential with an average condensate density of $n_B = 0.9 \times 10^{14} \text{ cm}^{-3}$. This determines the system energy scale $E_n = \hbar^2 k_n^2 / 2m$ through the wave number $k_n = (6\pi^2 n_B)^{1/3}$ and importantly sets the relevant timescale $t_n = \hbar / E_n = 4 \mu\text{s}$. We employ a second hyperfine state $|F = 1, m_F = 0\rangle$ as the impurity state. The interaction strength between the two states is characterized by the dimensionless parameter $1/k_n a$, where a is the interstate scattering length. This scattering length can be tuned by the magnetic field via a Feshbach resonance located at 113.8 G [23,24]. The medium scattering length is $a_B \approx 9a_0$, where a_0 is the Bohr radius, and is approximately constant for the applied magnetic fields

An interferometric sequence consisting of two radio-frequency (rf) pulses is employed, which allows us to populate an impurity state and probe the subsequent dynamics. Similar interferometric investigations have previously explored impurity dynamics in a Fermi

gas [8,9] and motional coherence of fixed impurities in a BEC [25,26]. The rf pulses are resonant with the atomic transition and their short duration of $0.5 \mu\text{s}$ allows the dynamics to be well resolved. The first rf pulse quenches the system into a superposition of the impurity state and the medium state corresponding to a $\sim 5\%$ population in the former, which ensures vanishing interaction between the impurities [20]. The system then evolves for a variable time t , in which the phase of the coherence advances and the coherence amplitude decays due to interactions between the two states. Finally, a second rf pulse probes the system with a variable phase φ . Subsequently, the atoms are held in the dipole trap for an additional 2 ms where three-body losses remove two medium atoms for each impurity. Thus, only medium atoms remain whose number is inversely proportional to the number of impurity atoms after the second rf pulse. After free expansion the remaining number of the medium state atoms is measured through absorption imaging.

This resulting atom number depends sinusoidally on the probe phase and for each evolution time t we perform a fit $N(\varphi) = N_0 - \mathcal{A} \cos(\varphi - \varphi_C)$. Here, the amplitude \mathcal{A} corresponds to the extent to which the coherence is preserved and φ_C corresponds to the phase acquired during the evolution time t . Thus, we obtain the amplitude $|C(t)| = |\mathcal{A}(t)/\mathcal{A}(0)|$ and the phase φ_C of the coherence for each chosen interaction strength and evolution time. Example measurements of the coherence amplitude and phase are shown in Figure 2 for weak and unitary interactions (Slight differences in the data with respect to Ref. [20] arise due to an improved calibration of the imaging system.). These measurements clearly display how the coherence of the system evolves as time progresses between the two rf pulses.

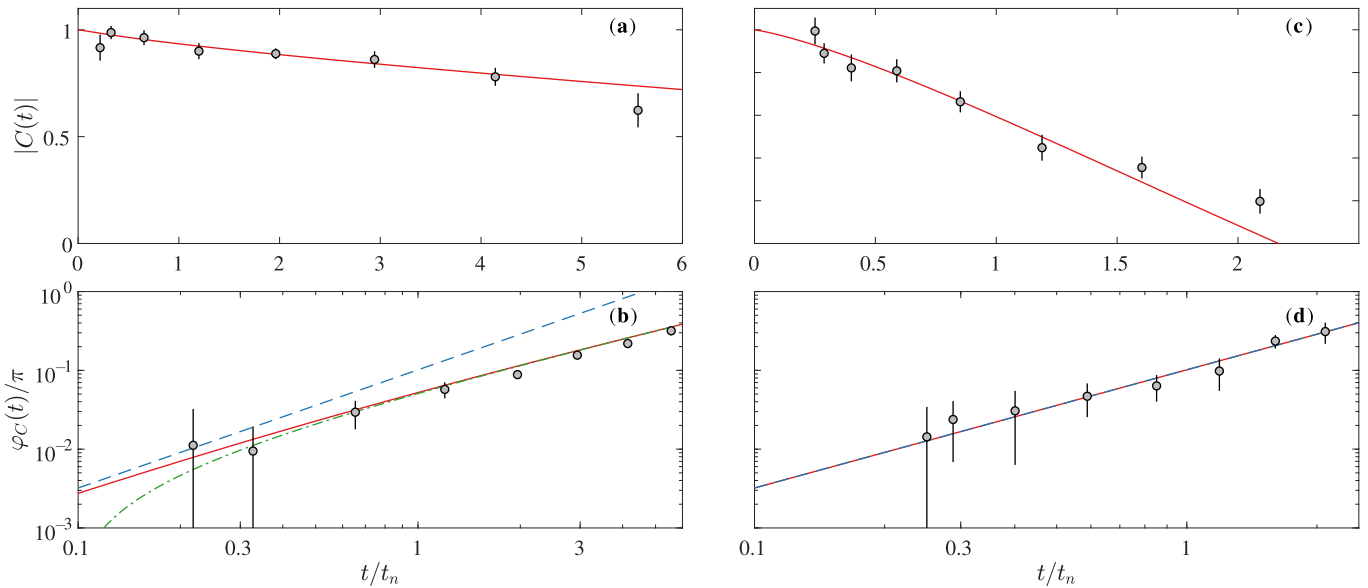


Figure 2. Two-body dynamics at weak and unitary interaction strengths. The coherence amplitude (top row) and phase evolution (bottom row) at $1/k_n a = -1.8$ (a,b) and $1/k_n a = 0.01$ (c,d). The corresponding data were previously presented in Ref. [20]. Equation (1) is shown as a solid red line and the two limits in Equation (2) are shown as a dashed blue line and a dash-dotted green line for the universal and the weak coupling dynamics, respectively. Note that the universal description coincides with the general two-body model in panel (d). The errors correspond to fit uncertainties.

3. Two-Body Regimes of Dynamical Evolution

In the following section we briefly outline the theoretical description of the dynamical regimes which we compare with our experimental results. A short-time theoretical prediction can be obtained from the spectral function of the impurity. This describes the impurity in the frequency-domain and generally contains a polaron ground state and a continuum of excited states. Though the exact spectral function at arbitrary interaction strength has no general solution, the tail of excited states at high frequencies has previously

been investigated in detail [27]. Due to the intrinsic link between frequency-domain and time-domain behavior, the Fourier transform of this high-frequency solution yields the coherence for the initial two-body dynamics. For low medium-medium scattering length, it can be expressed as [20]

$$C(t) \simeq 1 - i \frac{E_{\text{mf}} t}{\hbar} + \frac{2}{3\pi} (k_n |a|)^3 \left[1 - \frac{2}{\sqrt{\pi}} e^{it/t_a} \Gamma\left(\frac{3}{2}, i \frac{t}{t_a}\right) \right], \quad (1)$$

where Γ is the incomplete gamma function, $E_{\text{mf}} = 4\pi\hbar^2 n_B a / m$ is the mean-field energy and $t_a = ma^2 / \hbar$ is the timescale set by the medium-impurity scattering length a . The coherence amplitude and phase can be examined using the coherence in the small-angle approximation. Thus, to the lowest order, the experimentally measured amplitude and phase correspond to the real and imaginary part of Equation (1).

Remarkably, this two-body prediction is exact for any interaction strength from weak to strong interactions [20]. Furthermore, it is possible to simplify Equation (1) in the following limits

$$C(t) = \begin{cases} 1 - (1 - i) \frac{16}{9\pi^{3/2}} \left(\frac{t}{t_n}\right)^{3/2} & t \ll t_a \\ 1 - i E_{\text{mf}} t / \hbar - (1 + i) \left(\frac{t}{t_w}\right)^{1/2} & t \gg t_a \end{cases} \quad (2)$$

where $t_w = m / 32\pi\hbar n_B^2 a^4$. The long-time limit of the equation is valid to second order in the impurity-medium scattering length a , and it can be extended to include a third-order correction [20]. Furthermore, it clearly demonstrates two distinct regimes. At short times $t \ll t_a$ the high-frequency scattering is limited by the density and the coherence evolves with an interaction independent timescale t_n and an exponent of $3/2$. For longer times $t \gg t_a$, this transitions into weak coupling dynamics marked by the appearance of the mean-field energy, the interaction dependent timescale t_w , and the exponent $1/2$.

These power laws reflect the behavior of the scattering cross section $\sigma(k) = 4\pi a^2 / [1 + (ka)^2]$ in the two regimes [20]. In a simple picture, it governs the collision rate, which we assume to equal the rate of decoherence $\dot{C}(t) \sim -n_B \sigma v$. At a given time t during the evolution after the first rf pulse, the characteristic energy associated with decoherence is $E \sim \hbar/t$, which sets the wave number $k \sim \sqrt{m/\hbar t}$ and collisional velocity $v \sim \sqrt{\hbar/mt}$. For short times $t \ll t_a$, the cross section is unitary-limited $\sigma \sim 1/k^2 \sim \hbar t / m$. By integrating the corresponding rate of decoherence we obtain $C(t) \sim (t/t_n)^{3/2}$, which precisely reflects the universal limit of Equation (2). In contrast, for longer times $t \gg t_a$ the cross section is dominated by the scattering length as $\sigma \sim a^2$. Integrating the decoherence rate here yields the weak coupling limit $C(t) \sim (t/t_w)^{1/2}$. The timescale t_a is therefore key in describing which regime governs the dynamical evolution of the system.

4. Coherence Amplitude and Phase Evolution

Based on the experiment described in Section 2, it is possible to observe the evolution of an impurity state by monitoring the coherence amplitude $|C|$ and phase φ_C . Here we compare such measurements with the theoretical prediction from Section 3. Examples of measured coherence amplitude and phase are shown in Figure 2 for weak and resonant interactions with the general two-body description (Equation (1)) for all panels and with its limits (Equation (2)) for the phase.

For both data sets, the coherence amplitude decreases as function of evolution time, driven by the dynamical scattering events. This shows that the impurity state evolves and loses coherence with the initial state (To compare the experimental observations with this prediction, the coherence amplitude is normalized by fitting Equation (1) with an overall amplitude within t_n .) at a rate which increases for large interaction strengths as expected.

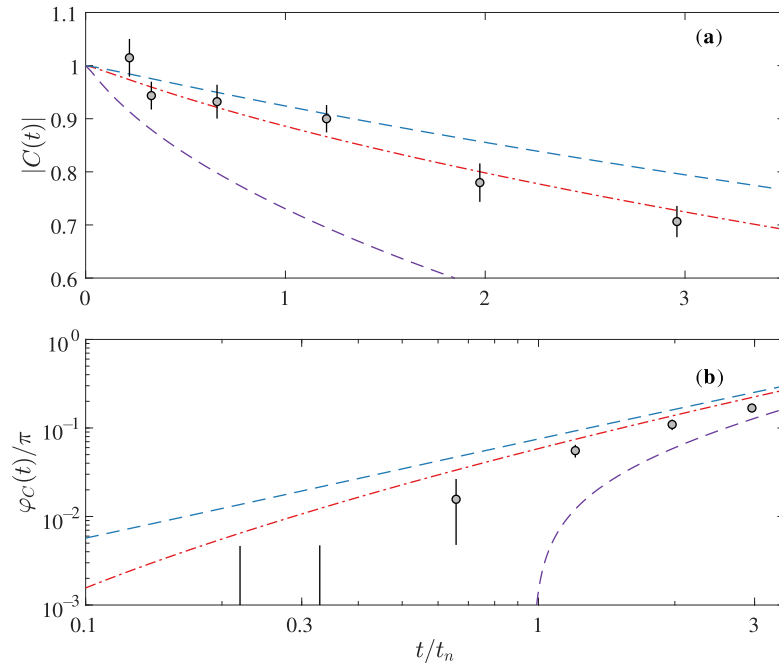


Figure 3. Transition from universal to weak coupling dynamics. (a) The coherence amplitude and (b) phase evolution at $1/k_n a = -1.3$ (circles) with Equation (1) as a dash-dotted line for its fitted value $t_a = 0.2t_n$ (red) and as dashed lines using two additional values $0.05t_n$ (purple) and $0.5t_n$ (blue). The errors correspond to fit uncertainties.

The coherence amplitude in the upper panels of Figure 2 is affected by additional decoherence processes which all contribute to its gradual decay. To accurately model the experiment, we therefore include effects stemming from the inhomogeneous density distribution, the lifetime of the impurity and shot-to-shot magnetic field fluctuations in our theoretical description. The dephasing due to the inhomogeneous density distribution is accounted for by integration of the coherence over the density distribution of the BEC. This is modeled in the Thomas–Fermi limit using a parabolic density profile. The lifetime of the impurity due to recombination was measured independently and included by multiplying the coherence with an exponential decay. The lifetime ranges from $\sim 7t_n$ at unitarity to $\sim 42t_n$ at weak interaction strengths. The shot-to-shot magnetic field fluctuations were also measured independently and incorporated in the theoretical description of the coherence. This was achieved by multiplying the coherence with the integrated distribution of phases caused by the slight differences in the magnetic field at each experimental repetition. Since the temperature of the cloud was ~ 50 nK, the corresponding thermal timescale $\hbar/k_B T \sim 38t_n$ is beyond the accessible regime of impurity dynamics and thus thermal effects are negligible. The resulting two-body prediction is illustrated in Figure 2 and clearly agrees with the data for short times. Since no fitting parameters are employed, the excellent agreement of the prediction and observations highlights that the theory captures the dynamical behavior of the system exceedingly well.

The lower panels of Figure 2 show the evolution of the coherence phase as a function of time, where a faster evolution is observed for larger interaction strengths. Since the experimental decoherence mechanisms primarily influence the coherence amplitude, the phase is better suited to observe the power-law behavior of the coherence evolution. It is therefore plotted in a double logarithmic fashion (Note that the coherence phase cannot be reliably extracted for long evolution times due to the vanishing coherence amplitude.). The imaginary part of Equation (1) is also shown in the lower panels of Figure 2 in good agreement with the observations. To gain further insight, we show the limits of Equation (2) as well. For weak interactions (Figure 2b) the transition from two-body universal dynamics to weak coupling dynamics occurs almost immediately and the $\sim t^{1/2}$ limit of Equation (2) captures the entire observed phase evolution. At unitarity, the universal dynamics extends

to much longer evolution times and thus the $\sim t^{3/2}$ limit of Equation (2) coincides with Equation (1) and agrees with the experimental observations.

In general, it is remarkable how well the measured coherence amplitude and phase at short times agree with Equation (1) considering the wide span of interaction strengths from weak to unitary. Moreover, our result shows that the limits of Equation (2) are valid and allow a clear distinction of the two regimes. This consolidates our understanding of the initial two-body dynamics and validates the theoretical prediction.

5. Transition from Universal to Weak Coupling Dynamics

Equation (2) shows that the transition between the universal and the weak coupling regime is given by t_a , which sets an important timescale of the dynamics and motivates its experimental investigation. In the following we show that the transition time can be extracted from the observations with a model-dependent fit and discuss the fitted results as function of interaction strength.

The transition time t_a appears in the general short-time prediction Equation (1) as an interaction dependent timescale. We therefore fit Equation (1) simultaneously to the coherence amplitude and phase evolution with t_a as the only free parameter to extract the transition between the two regimes. Importantly, we only fit the initial data of each set since Equation (1) is only valid in the limit of short times. The fitted timescales at four interaction strengths are shown in Figure 1a together with the predicted transition times between the dynamical regimes. The extracted transition time increases for stronger interactions indicating an extended evolution time of universal dynamics. Moreover, the timescale is in clear agreement with the predicted value of t_a .

Remarkably, the fitted value and its error are small compared with the dynamical timescale t_n . Since the duration of the probing pulses is $0.5 \mu\text{s} \sim 0.1t_n$, it is not immediately clear that such small timescales can be extracted experimentally. To illustrate the feasibility, a fit at $1/k_na = -1.3$ is shown in Figure 3, which yields an extracted transition time of $0.2(2)t_n$ in agreement with the predicted value of $t_a = 0.3t_n$. Additionally, two lines are shown where $t_a = 0.05t_n$ and $0.5t_n$. This figure thus clarifies that t_a affects the functional shape of the coherence at times much larger than its own value. Therefore, even small differences in t_a cause large discrepancies when compared with the experimental observation, which is most pronounced for the coherence amplitude Figure 3a.

We thus demonstrate that a transition time can be extracted experimentally in agreement with theoretical predictions. For sufficiently large interaction strengths $|1/k_na| \lesssim 0.5$, a transition to weak coupling dynamics is not observable, since the many-body regime is entered directly.

6. Two-Body Exponent and Time Constant

The limits given by Equation (2) show that the universal and weak coupling regime display distinctively different functional behavior corresponding to power-law exponents $3/2$ and $1/2$, respectively. We now turn our attention to the investigation of this functional difference by fitting such a power law to the coherence amplitude and observing its dependence on the interaction strength.

The two limits of the two-body prediction in Equation (2) are especially simple for the coherence amplitude and follow the form $1 - (t/t_c)^\beta$. For weak coupling dynamics $\beta = 1/2$ and t_c is interaction dependent whereas for universal dynamics $\beta = 3/2$ and t_c is constant. By fitting a power law to the coherence amplitude within the regimes of two-body dynamics, the fitted values of β and t_c can indicate the functional behavior at the chosen interaction strength.

The fitted exponents and time constants are shown in Figure 4 together with the weak coupling and universal values. For low interaction strengths β agrees with the prediction of weak coupling dynamics. At stronger interactions it slowly increases and reaches $3/2$ at unitarity in agreement with the universal prediction. The fitted time constant t_c initially decreases for increasing interaction strength and qualitatively follows the behavior of

the predicted timescale t_w of weak coupling dynamics. However, for strong interaction strengths, where t_w diverges, t_c remains finite and connects with the universal value of $\sim 2.1t_n$. The error bars correspond to symmetric fit uncertainties and the apparent asymmetry is due to the logarithmic scale.

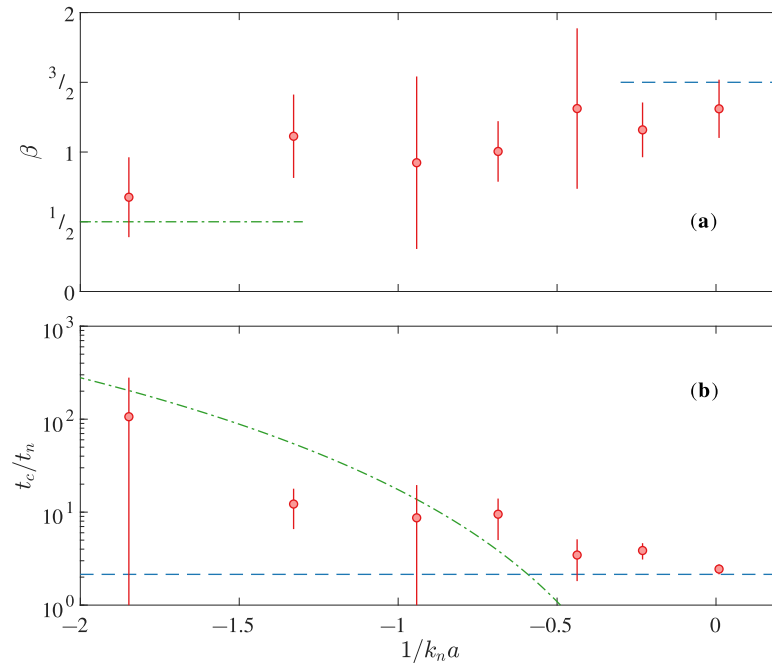


Figure 4. Characteristic exponent and time constant. By fitting a power law $1 - (t/t_c)^\beta$ to the coherence amplitude, we obtain the characteristic exponent (a) and time constant (b) at various interaction strengths. The theoretically predicted exponent and time constants for universal and weak coupling dynamics are shown as a dashed blue line and a dash-dotted green line, respectively. The errors correspond to fit uncertainties.

The experimental observations in the transition region between weak and unitary interactions are influenced by the behavior of both two-body regimes. Therefore, the specific values of β and t_c bear no physical meaning and are a consequence of fitting a single time dependence to the data when both weak coupling and universal dynamics are present. Nonetheless, at weak and unitary interactions the fitted power law is dominated by either one of the two-body regimes and we observe a smooth connection between the two in the transition region.

7. Conclusions

The results presented here provide a detailed investigation of the initial two-body dynamics of a quantum impurity in a BEC. The impurity dynamics has previously been studied [20], and here we have extended the analysis of the initial universal and subsequent weak coupling dynamics and the transition between them.

An interferometric sequence was used to measure the coherence of the system quenched into a superposition of an impurity state and a medium state. The evolution of the coherence was predicted by a rigorous short-time model, which showed a universal and a weak coupling regime with distinct exponents and timescales. A direct comparison between the experimental observations and the two-body theoretical prediction confirmed the validity of the model.

The transition between the two regimes was analyzed at four interaction strengths yielding transition times in clear agreement with the theoretical prediction as shown in Figure 1. Additionally, the transition was investigated by fitting a power law to the coherence amplitude, revealing how the exponent and time constant change from weak coupling to universal dynamics for increasing interaction strength.

These investigations improve our understanding of the fundamental properties of quasiparticles. By comparing interferometric observations at long evolution times to earlier spectroscopic results [14–17] a complete model for the Bose polaron in both time and frequency-domain can be obtained. Furthermore, the experimental methods may be expanded to help elucidate exotic phenomena such as transport processes [28,29] or dynamical formation of bipolarons [30].

Author Contributions: Conceptualization, M.G.S., T.G.S., N.B.J. and J.J.A.; methodology, M.G.S.; software, M.G.S.; validation, M.G.S., T.G.S., N.B.J. and J.J.A.; formal analysis, M.G.S.; investigation, M.G.S., T.G.S., N.B.J. and J.J.A.; resources, J.J.A.; data curation, M.G.S.; writing—original draft preparation, M.G.S.; writing—review and editing, M.G.S., T.G.S., N.B.J. and J.J.A.; visualization, M.G.S.; supervision, J.J.A.; project administration, J.J.A.; funding acquisition, J.J.A. All authors have read and agreed to the published version of the manuscript.

Funding: This work has been supported by the Danish National Research Foundation through the Center of Excellence “CCQ” (Grant agreement no.: DNRF156).

Institutional Review Board Statement: Not applicable.

Informed Consent Statement: Not applicable.

Data Availability Statement: The data that support the findings of this study are available from the corresponding author upon reasonable request.

Acknowledgments: We thank K. K. Nielsen, A. Camacho-Guardian, T. Pohl, and G. M. Bruun for helpful discussions.

Conflicts of Interest: The authors declare no conflict of interest.

References

1. Landau, L.D.; Pekar, S.I. Effective mass of a polaron. *Zh. Eksp. Teor. Fiz.* **1948**, *18*, 419–423.
2. Devreese, J.T.; Alexandrov, A.S. Fröhlich polaron and bipolaron: Recent developments. *Rep. Prog. Phys.* **2009**, *72*, 066501. [[CrossRef](#)]
3. Gershenson, M.E.; Podzorov, V.; Morpurgo, A.F. *Colloquium: Electron. Transp. Single-Cryst. Org. Rev. Mod. Phys.* **2006**, *78*, 973–989. [[CrossRef](#)]
4. Dagotto, E. Correlated electrons in high-temperature superconductors. *Rev. Mod. Phys.* **1994**, *66*, 763–840. [[CrossRef](#)]
5. Schirotzek, A.; Wu, C.H.; Sommer, A.; Zwierlein, M.W. Observation of Fermi polarons in a tunable Fermi liquid of ultracold atoms. *Phys. Rev. Lett.* **2009**, *102*, 230402. [[CrossRef](#)] [[PubMed](#)]
6. Kohstall, C.; Zaccanti, M.; Jag, M.; Trenkwalder, A.; Massignan, P.; Bruun, G.M.; Schreck, F.; Grimm, R. Metastability and coherence of repulsive polarons in a strongly interacting Fermi mixture. *Nature* **2012**, *485*, 615–618. [[CrossRef](#)]
7. Koschorreck, M.; Pertot, D.; Vogt, E.; Fröhlich, B.; Feld, M.; Köhl, M. Attractive and repulsive Fermi polarons in two dimensions. *Nature* **2012**, *485*, 619–622. [[CrossRef](#)]
8. Cetina, M.; Jag, M.; Lous, R.S.; Walraven, J.T.M.; Grimm, R.; Christensen, R.S.; Bruun, G.M. Decoherence of Impurities in a Fermi Sea of Ultracold Atoms. *Phys. Rev. Lett.* **2015**, *115*, 135302. [[CrossRef](#)]
9. Cetina, M.; Jag, M.; Lous, R.S.; Fritsche, I.; Walraven, J.T.; Grimm, R.; Levinsen, J.; Parish, M.M.; Schmidt, R.; Knap, M.; et al. Ultrafast many-body interferometry of impurities coupled to a Fermi sea. *Science* **2016**, *354*, 96–99. [[CrossRef](#)] [[PubMed](#)]
10. Scazza, F.; Valtolina, G.; Massignan, P.; Recati, A.; Amico, A.; Burchianti, A.; Fort, C.; Inguscio, M.; Zaccanti, M.; Roati, G. Repulsive Fermi Polarons in a Resonant Mixture of Ultracold ⁶Li Atoms. *Phys. Rev. Lett.* **2017**, *118*, 083602. [[CrossRef](#)]
11. Schmidt, R.; Knap, M.; Ivanov, D.A.; You, J.S.; Cetina, M.; Demler, E. Universal many-body response of heavy impurities coupled to a Fermi sea: A review of recent progress. *Rep. Prog. Phys.* **2018**, *81*, 024401. [[CrossRef](#)]
12. Yan, Z.; Patel, P.B.; Mukherjee, B.; Fletcher, R.J.; Struck, J.; Zwierlein, M.W. Boiling a Unitary Fermi Liquid. *Phys. Rev. Lett.* **2019**, *122*, 093401. [[CrossRef](#)]
13. Darkwah Oppong, N.; Riegger, L.; Bettermann, O.; Höfer, M.; Levinsen, J.; Parish, M.M.; Bloch, I.; Fölling, S. Observation of Coherent Multiorbital Polarons in a Two-Dimensional Fermi Gas. *Phys. Rev. Lett.* **2019**, *122*, 193604. [[CrossRef](#)]
14. Jørgensen, N.B.; Wacker, L.; Skalmstang, K.T.; Parish, M.M.; Levinsen, J.; Christensen, R.S.; Bruun, G.M.; Arlt, J.J. Observation of Attractive and Repulsive Polarons in a Bose-Einstein Condensate. *Phys. Rev. Lett.* **2016**, *117*, 055302. [[CrossRef](#)] [[PubMed](#)]
15. Hu, M.G.; Van de Graaff, M.J.; Kedar, D.; Corson, J.P.; Cornell, E.A.; Jin, D.S. Bose Polarons in the Strongly Interacting Regime. *Phys. Rev. Lett.* **2016**, *117*, 055301. [[CrossRef](#)]
16. Peña Ardila, L.A.; Jørgensen, N.B.; Pohl, T.; Giorgini, S.; Bruun, G.M.; Arlt, J.J. Analyzing a Bose polaron across resonant interactions. *Phys. Rev. A* **2019**, *99*, 063607. [[CrossRef](#)]

17. Yan, Z.Z.; Ni, Y.; Robens, C.; Zwierlein, M.W. Bose polarons near quantum criticality. *Science* **2020**, *368*, 190–194. [[CrossRef](#)] [[PubMed](#)]
18. Catani, J.; Lamporesi, G.; Naik, D.; Gring, M.; Inguscio, M.; Minardi, F.; Kantian, A.; Giamarchi, T. Quantum dynamics of impurities in a one-dimensional Bose gas. *Phys. Rev. A* **2012**, *85*, 023623. [[CrossRef](#)]
19. Meinert, F.; Knap, M.; Kirilov, E.; Jag-Lauber, K.; Zvonarev, M.B.; Demler, E.; Nägerl, H.C. Bloch oscillations in the absence of a lattice. *Science* **2017**, *356*, 945–948. [[CrossRef](#)]
20. Skou, M.G.; Skov, T.G.; Jørgensen, N.B.; Nielsen, K.K.; Camacho-Guardian, A.; Pohl, T.; Bruun, G.M.; Arlt, J.J. Non-equilibrium quantum dynamics and formation of the Bose polaron. *Nat. Phys.* **2021**. [[CrossRef](#)]
21. Parish, M.M.; Levinsen, J. Quantum dynamics of impurities coupled to a Fermi sea. *Phys. Rev. B* **2016**, *94*, 184303. [[CrossRef](#)]
22. Wacker, L.J.; Jørgensen, N.B.; Birkmose, D.; Winter, N.; Mikkelsen, M.; Sherson, J.; Zinner, N.; Arlt, J.J. Universal Three-Body Physics in Ultracold KRb Mixtures. *Phys. Rev. Lett.* **2016**, *117*, 163201. [[CrossRef](#)]
23. Lysebo, M.; Veseth, L. Feshbach resonances and transition rates for cold homonuclear collisions between ^{39}K and ^{41}K atoms. *Phys. Rev. A* **2010**, *81*, 032702. [[CrossRef](#)]
24. Tanzi, L.; Cabrera, C.R.; Sanz, J.; Cheiney, P.; Tomza, M.; Tarruell, L. Feshbach resonances in potassium Bose-Bose mixtures. *Phys. Rev. A* **2018**, *98*, 062712. [[CrossRef](#)]
25. Scelle, R.; Rentrop, T.; Trautmann, A.; Schuster, T.; Oberthaler, M.K. Motional Coherence of Fermions Immersed in a Bose Gas. *Phys. Rev. Lett.* **2013**, *111*, 070401. [[CrossRef](#)] [[PubMed](#)]
26. Rentrop, T.; Trautmann, A.; Olivares, F.A.; Jendrzejewski, F.; Komnik, A.; Oberthaler, M.K. Observation of the Phononic Lamb Shift with a Synthetic Vacuum. *Phys. Rev. X* **2016**, *6*, 041041. [[CrossRef](#)]
27. Braaten, E.; Kang, D.; Platter, L. Short-Time Operator Product Expansion for rf Spectroscopy of a Strongly Interacting Fermi Gas. *Phys. Rev. Lett.* **2010**, *104*, 223004. [[CrossRef](#)]
28. Sommer, A.; Ku, M.; Zwierlein, M.W. Spin transport in polaronic and superfluid Fermi gases. *New J. Phys.* **2011**, *13*, 055009. [[CrossRef](#)]
29. Bardon, A.B.; Beattie, S.; Luciuk, C.; Cairncross, W.; Fine, D.; Cheng, N.S.; Edge, G.J.A.; Taylor, E.; Zhang, S.; Trotzky, S.; et al. Transverse Demagnetization Dynamics of a Unitary Fermi Gas. *Science* **2014**, *344*, 722–724. [[CrossRef](#)] [[PubMed](#)]
30. Camacho-Guardian, A.; Peña Ardila, L.A.; Pohl, T.; Bruun, G.M. Bipolarons in a Bose-Einstein Condensate. *Phys. Rev. Lett.* **2018**, *121*, 013401. [[CrossRef](#)]